

Figure S1

Figure S1, Related to Figure 1.

(A, left) Lysates of the cells expressing H2B-PA-mCherry were subjected to sodium dodecyl sulfate-polyacrylamide gel electrophoresis (SDS-PAGE), and subsequent Coomassie brilliant blue (CBB) staining and Western blotting. Expression of H2B-PA-mCherry was detected by the anti-mCherry (RFP) antibody, but not the anti-H2B antibody. However, in the saturated blot **(A, right)**, a faint band of ~50 kDa, corresponding to H2B-PA-mCherry, was detected by the anti-H2B antibody. The expression level of H2B-PA-mCherry was thus estimated at less than ~5% of endogenous H2B. **(B)** Single-step photobleaching of the nucleosome-PA-mCherry dots. The vertical axis represents the fluorescence intensity of each PA-mCherry dot. The horizontal axis is the tracking time series (photobleaching point is set as time 0; $n = 100$). The fluorescent intensity of each dot was approximately 75 and, in the single-step photobleaching profile, the intensity approached around 0, suggesting that each dot represents a single H2B-PA-mCherry molecule in a single nucleosome, as shown in (Funatsu et al., 1995; Sako et al., 2000). **(C)** A rare example of multiple (two)-step photobleaching of the H2B-PA-mCherry dots. First, the dot intensity of approximately 130 decreased to nearly half (~70) and then approached around 0. This two-step photobleaching indicates that the dot contains at least two H2B-PA-mCherry molecules. **(D)** The nuclei isolated from the HeLa cells expressing H2B-PA-mCherry were washed with the indicated buffers including various concentrations of NaCl. The resultant nuclear pellets (left) and supernatants (right) were subjected to SDS-PAGE, and subsequent CBB staining (upper) and Western blotting (bottom) with anti-mCherry and anti-H2B antibodies. Positions of histone H1 and core histones in CBB stain and H2B-PA-mCherry and H2B are indicated with arrows in the Western blot. Note that H2B and H2B-PA-mCherry started to dissociate from chromatin with 1 M NaCl and was detected in the supernatant fraction, suggesting that H2B-PA-mCherry was incorporated into nucleosome structures similar to endogenous H2B. **(E)** Point spread function (PSF) of observed H2B-PA-mCherry in a fixed HeLa cell. The xy-z kymograph shows that H2B-PA-mCherry can be detected in an optical layer with a thickness of ~200 nm. The vertical axis represents the depth of the optical layer (z plane) (50 nm/pixel), and the horizontal axis represents the xy plane (65 nm/pixel). **(F)** A simplified scheme for RDF and L-function analyses as a supplement to Figure 1F. A total of 49 particles were set in a clustered (red spheres, left top) or random manner (blue spheres, left bottom) around the origin point (black circle). Particles in the shell (middle top) and cumulative particles in the circle (middle bottom) were counted. The RDF (right top) and L-function (right bottom) plots were obtained by taking the ratio between actual density and random density from particles in the shell and cumulative particles in the circle, respectively. The horizontal axis represents the correlation distance (r). RDF and L-function plots of a random pattern (blue) were ~1 and 0, respectively. **(G)** An example of a random distribution (bottom) of particles is shown. Random distribution of dots was artificially generated at the same density as H2B actually observed in the nucleus. The bar represents 5 μm .

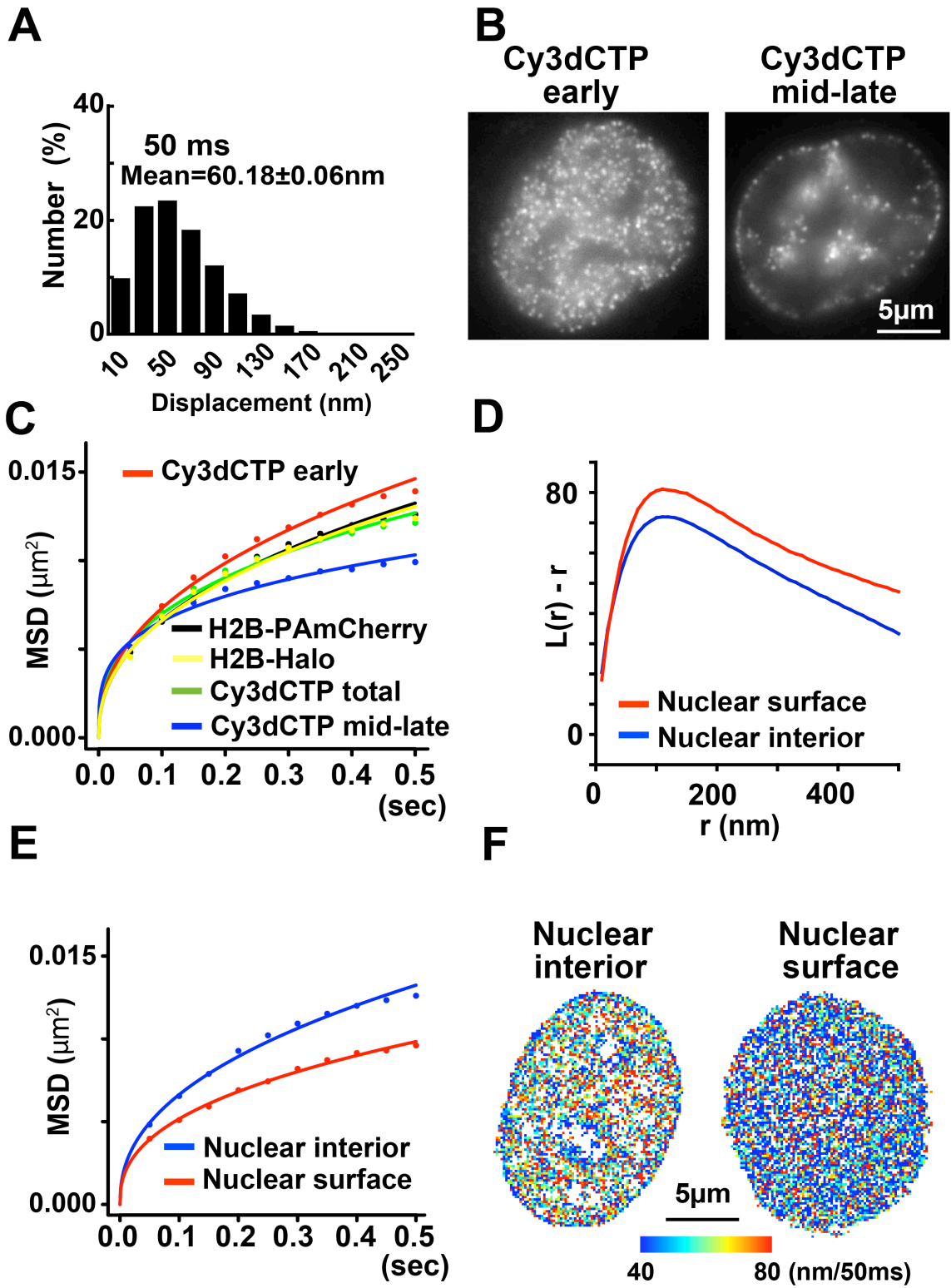


Figure S2

Figure S2, Related to Figure 2.

(A) Displacement (movement) distributions of single nucleosomes in the interphase chromatin of live HeLa cells for 50 ms ($n = 75$ cells). The mean \pm standard error for the 50 ms time point was indicated. **(B)** Representative images of early (left) and mid-late replication (right) foci labeled with Cy3-dCTP. **(C)** MSD plots for early (red) replication foci, mid-late replication (blue) foci, whole replication (green) foci, H2B-Halo (yellow), and H2B-PA-mCherry (black) from 0 to 0.5 s ($n = 15-75$ cells). Movements of H2B-Halo were tracked using the Fiji plug-in TrackMate. **(D)** L-function plots of chromatin on the nuclear periphery (red) and interior (blue). **(E)** MSD plots of chromatin on the nuclear periphery (red) and interior (blue). **(F)** Chromatin heat maps in a nucleoplasmic region and a nuclear periphery region for 50 ms. The color bar represents the scale of nucleosome movement in the heat map.

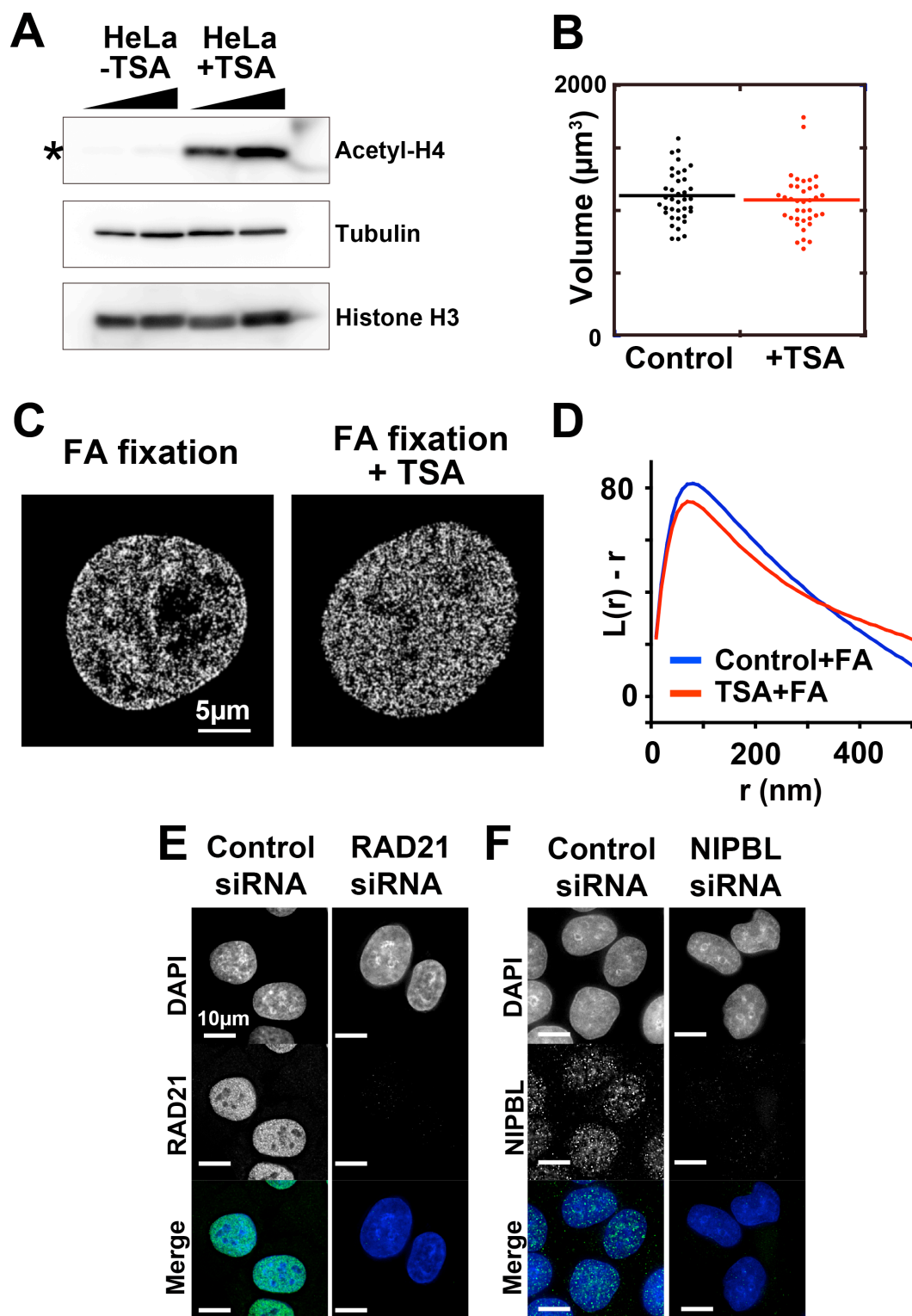


Figure S3

Figure S3, Related to Figure 3.

(A) Detection of histone H4 acetylation in HeLa cell lysates from TSA-treated cells (right) and untreated cells (left) by Western blotting with anti-acetylated H4 tail antibody. Note the specific increase in histone H4 acetylation in the TSA-treated cells. As controls, blotting results using anti-tubulin and anti-histone H3 antibodies are shown. **(B)** Effect of TSA on nuclear volume. HeLa cells were treated with 500 nM TSA for 2.5 h and then additionally treated with 0.5 $\mu\text{g}/\text{mL}$ Hoechst 33342 for 30 min. The z-stacked images of the labeled cell nuclei were observed using the Olympus FV-1000-D confocal laser scanning microscope (31 sections with a 500 nm thickness). The acquired z-stack images were analyzed by ImageJ plugin 3D Object Counter to measure the nuclear volume. For each condition, $n = 35$ cells. **(C)** PALM images of chromatin in a control FA-fixed cell and a TSA-treated FA-fixed cell. **(D)** L-function plots for a control FA-fixed cell (blue) and TSA-treated FA-fixed cell (red). TSA-treated FA-fixed cells show lower L-functions than those of control FA-fixed cells. **(E, F)** Verification of KD of the indicated chromatin-associated proteins by immunostaining: **E**, RAD21; **F**, NIPBL. The images show significant reductions in the target proteins compared to the control siRNA cells.

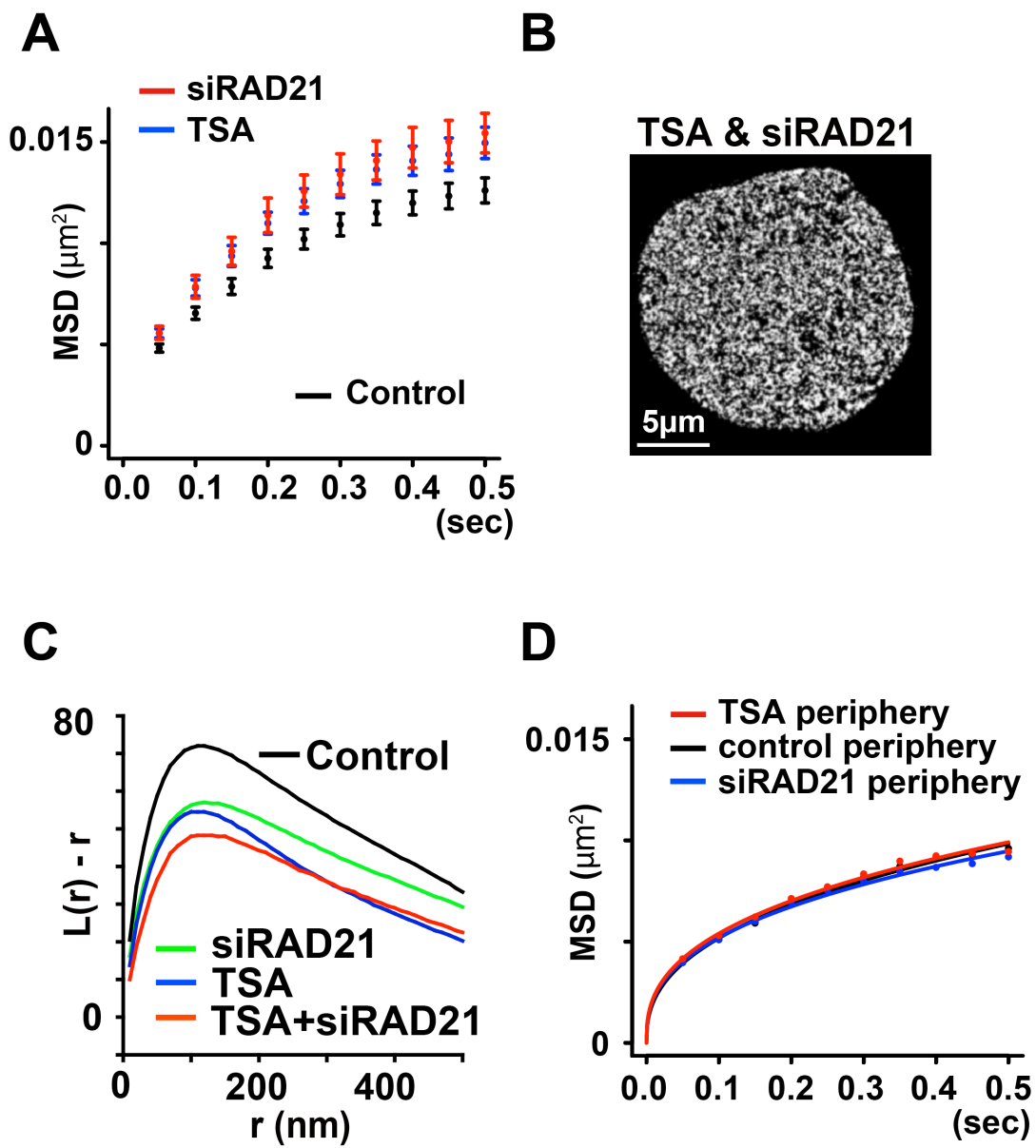


Figure S4

Figure S4, Related to Figure 3.

(A) MSD plots (\pm standard deviation [s.d.] among cells) of control, TSA-treated, and RAD21-KD domains. MSD of TSA-treated and RAD21-KD domains were significantly greater than the control (Kolmogorov–Smirnov, $p < 10^{-14}$ at all time points in control *vs.* TSA and control *vs.* RAD21-KD, error bars \pm s.d.). For each condition, $n = 25\text{--}75$ cells. **(B, C)** A representative PALM image **(B)** and L-function plots **(C)** of treatments with both TSA and RAD21-KD. **(D)** MSD plots of chromatin domains at the nuclear surface/periphery following treatment with TSA and RAD21-KD. Neither treatment was as effective on chromatin domains around the nuclear surface/periphery.

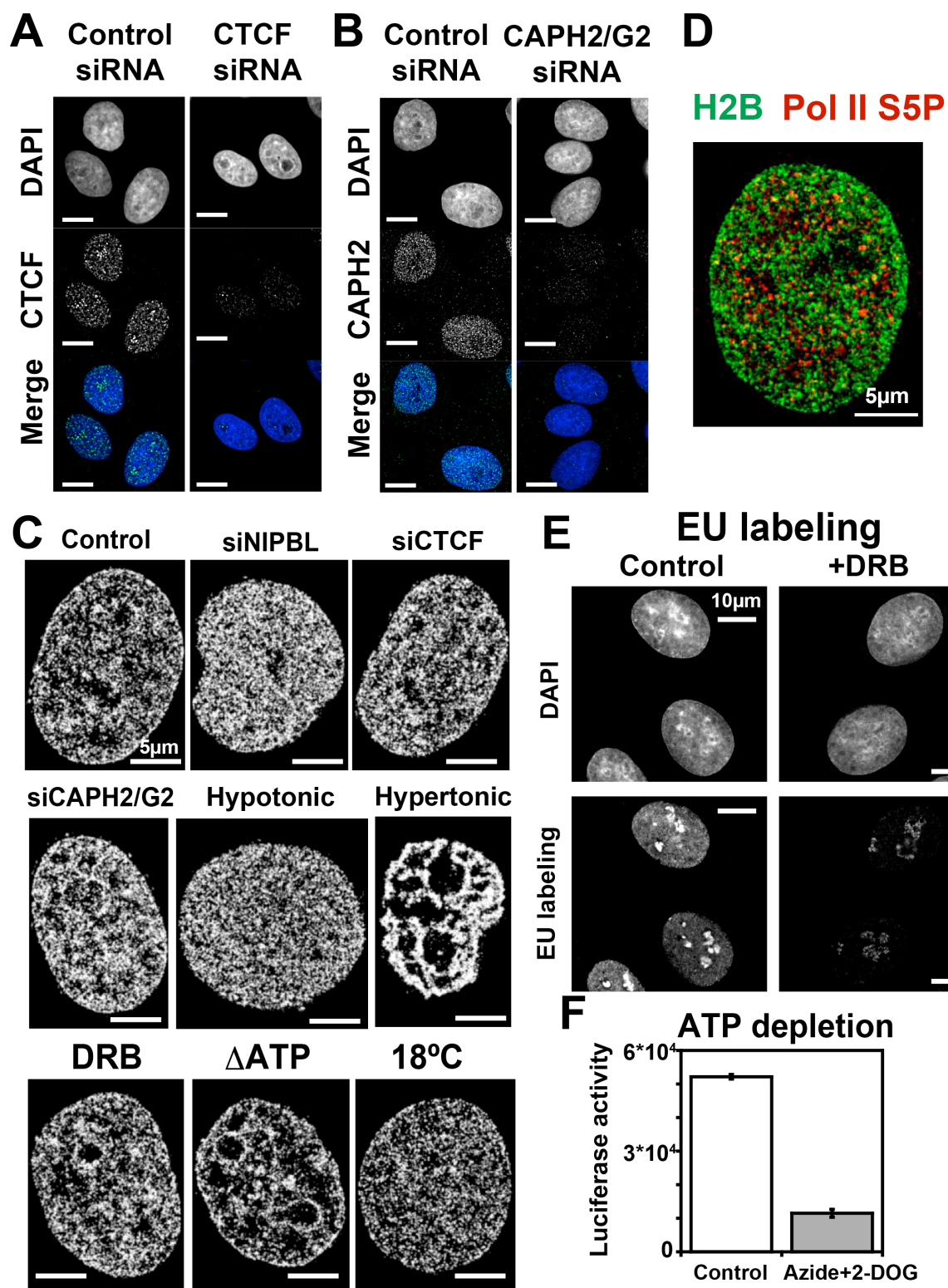


Figure S5

Figure S5, Related to Figure 4.

(A, B) Verification of KD of the indicated chromatin-associated proteins by immunostaining: **A**, CTCF and **B**, CAPH2/G2. The images show significant reductions in the target proteins compared to the control siRNA cells. The bar represents 10 μm . **(C)** PALM images of chromatin in a control (untreated) cell, NIPBL-KD cell, CTCF-KD cell, CAPH2/G2-KD cell, hypotonic cell, hypertonic cell, DRB cell, ATP-depleted cell (ΔATP), and cell cultured at room temperature (RT, 18°C). **(D)** Another example image of PALM (green) and Pol II phospho-Ser5 (red) staining. **(E)** EU labeling of newly synthesized RNA in control and DRB-treated cells. DRB treatment markedly decreased the efficiency of EU labeling. **(F)** Verification of ATP depletion based on luciferase activity, showing successful reduction of intracellular ATP level in cells treated with sodium azide and 2-deoxy-glucose (error bars \pm s.d.).

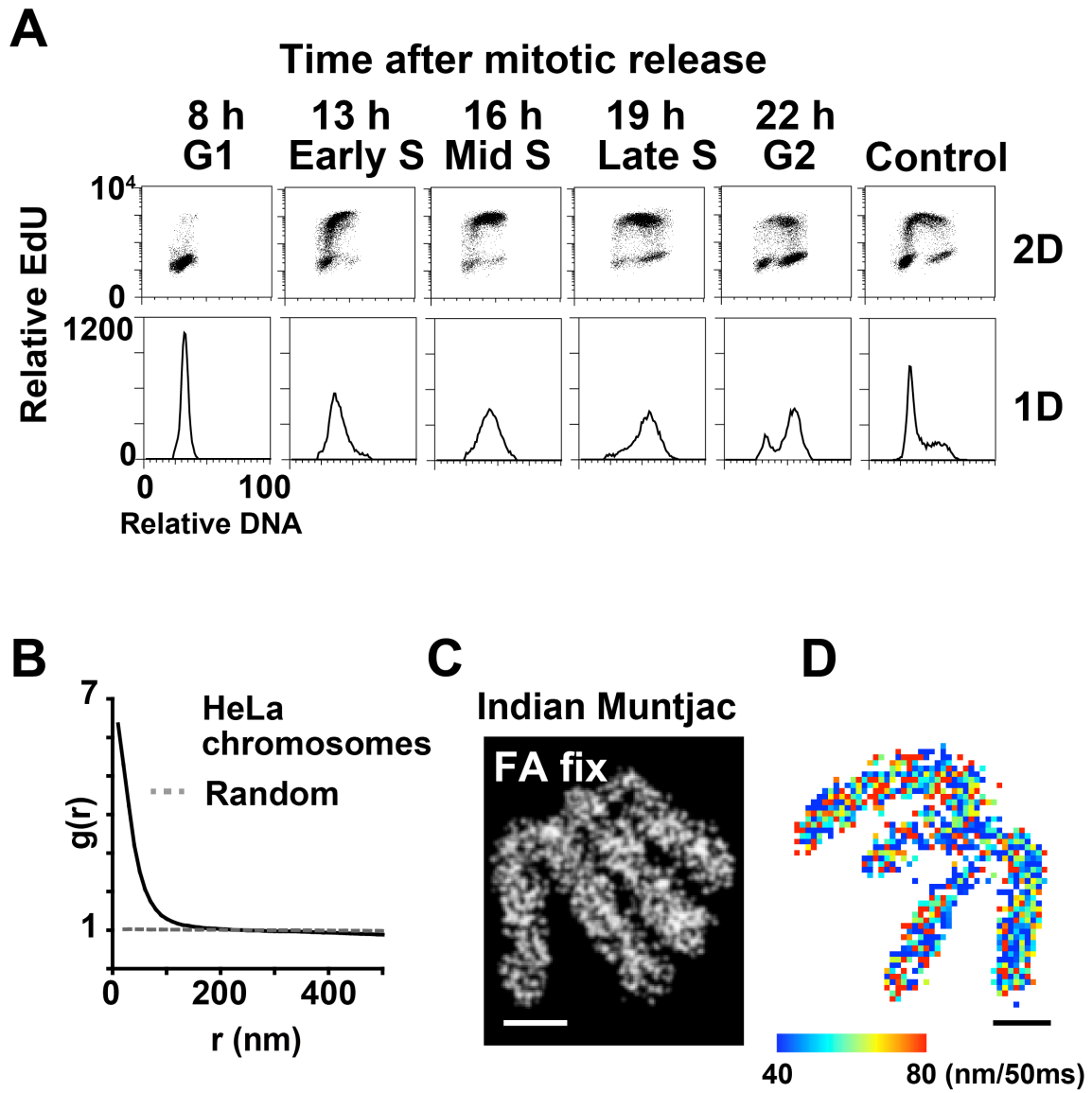


Figure S6

Figure S6, Related to Figure 5.

(A) To obtain cell cycle-synchronized cells, mitotic cells were collected using nocodazole arrest and mitotic shake-off, and cells were released in fresh medium. Each panel shows FACS profiles of synchronized cells at the indicated time point after release. To verify the cell cycle stages, labeling intensity with EdU to visualize DNA replication (vertical axis) and DNA content (horizontal axis) is shown. **(B)** The RDF plot of mitotic HeLa cells demonstrated that the nucleosomes indeed formed compact chromatin domains during mitosis. $n = 20$ cells. **(C)** PALM images of mitotic chromosomes in FA-fixed Muntjac DM cells. The bar represents 2 μm . **(D)** Heat map of Muntjac chromosomes. The color bar represents the scale of nucleosome movement in the heat map. The black bar represents 2 μm .

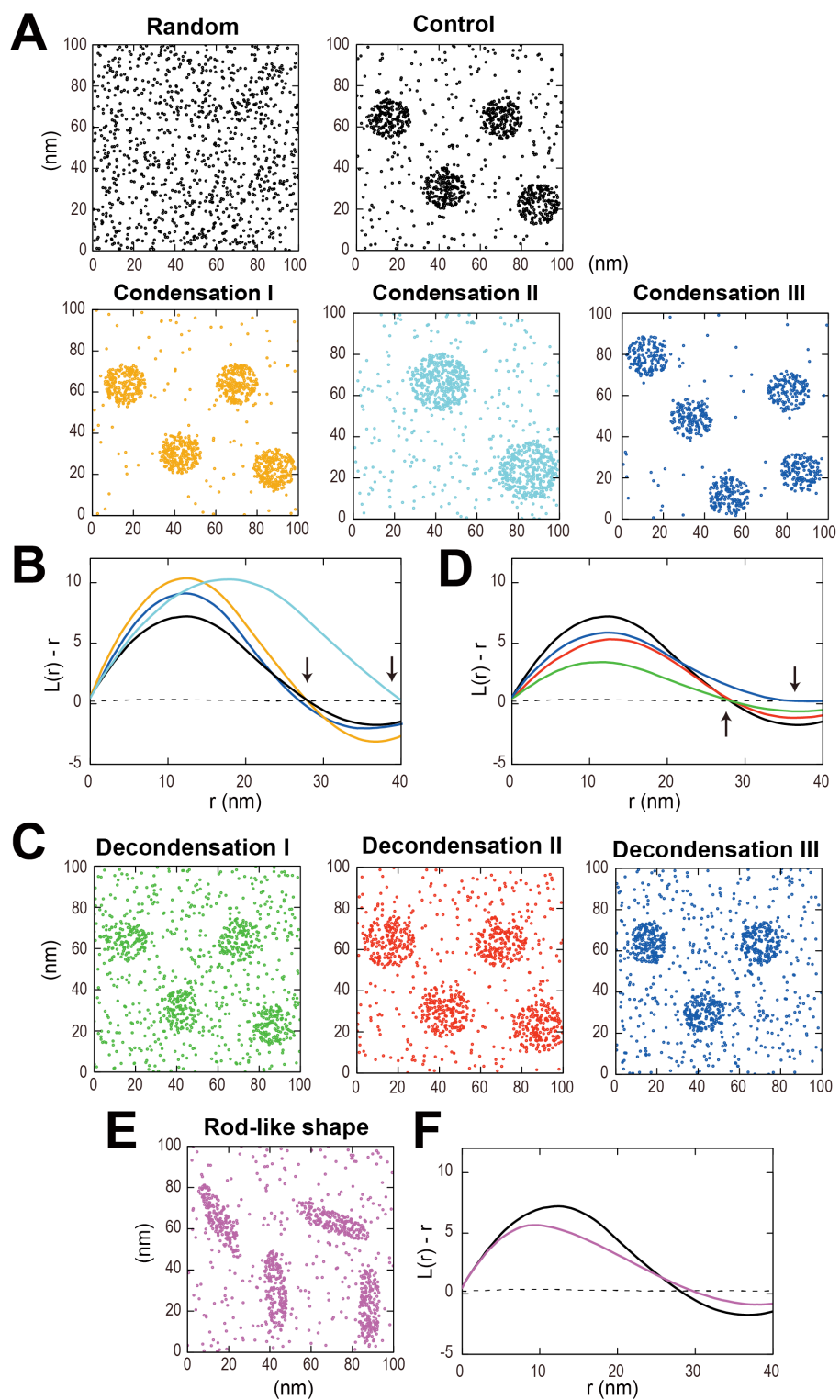


Figure S7

Figure S7, Related to Figures 1, 3-6.

L-function plots for three condensation, three decondensation and a rod-like shaped models. As described below, the modeling results suggest that the L-function peak can provide a good approximation of the size and compaction state of the domains. **(A)** The total number of dots in the square is constant at 1000. Random: 1000 dots are randomly distributed in the square. Control: ~75% of the dots are in the four domains, while 25% are outside the domains (radius = 10). Condensation I: the dot density in the domains is increased; ~90% of the dots are located in the four domains (radius = 10). Condensation II: ~75% of the dots are located in the two large domains (radius = 14.1), whose dot density is the same as that of the control. Condensation III: the number of domains (radius = 10) is increased from 4 to 5; the dot density in the domains is the same as that of the control. **(B)** L-function $[L(r)-r]$ plots for each condition are shown. The dotted line represents the random distribution of dots, and each plot color corresponds to the color of the models in (A). Note that with domain condensation, the L-function plots increased. The peak tails of the L-function plot (r values corresponding to $L(r)-r = 0$, marked with arrows) seem to be related to the domain spacing information. Where more domains had formed in the space, the r values were smaller. **(C)** The total number of dots in the square is constant at 1000. For Control, see panel (A). Decondensation I: the dot density in the domains is decreased; ~50% of the dots are located in the four domains (radius = 10). Decondensation II: ~75% of the dots are located in the four large domains (radius = 12.5), whose dot density is lower than that of the control. Decondensation III: the number of domains (radius = 10) is decreased from 4 to 3; the dot density in the domains is the same as the control. **(D)** L-function $[L(r)-r]$ plots for each condition are shown. The dotted line represents the random distribution of dots, and each plot color corresponds to the color in the models in (C). Note that with domain decondensation, the L-function of the plots decreased. The peak tails of the L-function plots (r values corresponding to $L(r)-r = 0$, marked with arrows) again seem to be related to the domain spacing information. Where less domains had formed in the space, the r values were larger. **(E)** A model for rod-like shaped domains expressed as ellipses. The total number of dots in the square is 1000, and the dot density in the domains is the same as that in the control (For Control, see panel (A)). The semi-minor and semi-major axes of the ellipses are 5 and 20, respectively. The dot density in the domains is the same as that in the control. **(F)** L-function $[L(r)-r]$ plot for rod-like shaped domains. Random and control plots are also shown. Note that the r value of the peak is smaller than that in the control.